Chemical Science

ROYAL SOCIETY OF CHEMISTRY

EDGE ARTICLE

View Article Online
View Journal | View Issue

Cite this: *Chem. Sci.*, 2026, **17**, 8043

All publication charges for this article have been paid for by the Royal Society of Chemistry

Jahn–Teller distortion controls electron transfer in photoexcited Cu(I) donor–acceptor systems

Pyosang Kim, *[a] Xinzheng Yang,[b] Brian T. Phelan, [a] Lars Kohler,[a] Karen L. Mulfort, *[a] Xiaosong Li *[b] and Lin X. Chen *[ac]

Received 30th December 2025
Accepted 20th February 2026

DOI: 10.1039/d5sc10209j

rsc.li/chemical-science

The Jahn–Teller distortion (JTD) is a defining structural response to electronic excitation in Cu(I)-based transition metal complexes, yet its role in photoinduced electron transfer (PET) remains largely unexplored. Here, we demonstrate that the JTD governs charge separation (CS) through a vibronically controlled conical intersection in heteroleptic Cu(I) bisphenanthroline–naphthalene diimide (CuHETPHEN-NDI) donor–acceptor dyads. Using 20-fs broadband transient absorption spectroscopy combined with coherent vibrational wavepacket (CVWP) analysis and quantum chemical calculations, we directly track nuclear motions that steer the system from the metal-to-ligand charge-transfer (^{1}MLCT) state to the CS state. Steric bulkiness of the pendant groups at the 2,9-positions of the phenanthroline ligand systematically slows both JTD and CS. Short-time Fourier transformation and Fourier filtering analyses identify two key vibrational signatures: a low-frequency breathing mode (~100 cm^{-1}) *via* a bond distance change between Cu and ligated Ns (Cu–N) that modulates the NDI anion absorption and acts as a vibronic coupling coordinate, and a higher-frequency mode (~313 cm^{-1}) that evolves along the PET trajectory. Normal mode analysis and potential energy surface calculations show that the JTD brings the ^{1}MLCT and CS states into degeneracy, while the Cu–N breathing motion dynamically modulates donor–acceptor electronic coupling to enable ultrafast nonadiabatic electron transfer. Steric hindrance exerted by the groups at the 2,9 positions of the phenanthroline ligands suppresses this vibronic coupling, leading to faster CVWP decoherence for the 313 cm^{-1} mode and slower CS. These findings unravel JTD-controlled vibronic coupling at conical intersection as a governing factor for CS and provide insight into designing Cu-based photosensitizers by harnessing structural dynamics to control PET.

Introduction

Transition metal complexes (TMCs) play important roles in a wide range of photoactivated applications, including light energy conversion,[1–3] and photocatalysis.[4–7] Upon photon absorption, these molecular systems frequently undergo charge-transfer (CT) in the excited states with redox properties, capable of initiating photoinduced electron transfer (PET), a fundamental process underlying these applications.[8] Thus, precise understanding of the excited state dynamics of the initially populated CT states in TMCs is essential for optimizing efficiency and achieving rational control over PET processes. Recent advances in ultrafast optical and X-ray spectroscopies, complemented by quantum-mechanical calculations, have revealed that CT excitation in TMCs drives the excited molecular structures far from thermal equilibrium, where electronic and nuclear motions become strongly coupled and nonadiabatic.[9–13] Therefore, deciphering PET reaction mechanisms need to consider not only thermally equilibrated MLCT state, but also their atomic position dependent energetics and dynamics in the potential energy surfaces. When the PET dynamics are comparable with certain vibrational motions of key reaction coordinates, it is important to investigate how nuclear motions in these vibrational modes influencing the reaction. These nuclear motions, especially in strong vibronic couplings cases in TMCs, can be detected through coherent vibrational wavepacket (CVWP) motions launched under the short pulse and broad band excitation due to simultaneously populating excited state vibronic manifold. These CVWP behaviors, *i.e.*, oscillation frequencies, nodes and dephasing time, can be related to excited state pathways, including intersystem crossing (ISC)[12–15] spin crossover,[9,10,16] transitions between different spin multiplicity. These CVWP motions can highlight nuclear dynamics that are vibronically driven by CT excitation, and actively reshape the excited state potential energy landscape.[17] However, it remains largely unclear how such photoinduced vibronic structural distortions of TMCs influence the PET reaction coordinate.

[a]*Chemical Sciences and Engineering Division, Argonne National Laboratory, Lemont, IL 60439, USA. E-mail: kimp@anl.gov; lchen@anl.gov*

[b]*Chemistry Department, University of Washington, Seattle, WA 98195, USA*

[c]*Chemistry Department, Northwestern University, Evanston, IL 60208, USA. E-mail: l-chen@northwestern.edu*

Photoinduced Jahn–Teller effect in TMCs[18,19] represents a fundamental mechanism linking electronic structure and molecular geometry in TMCs with partially filled d-orbitals. The Jahn–Teller distortion (JTD) drives geometric changes and lifts the electronic degeneracy and stabilize the complexes.[20] In 3d TMCs, the photoinduced Jahn–Teller effect often accompany CT excitation, giving rise to photophysical[21–23] and magnetic[24–28] properties. As such, the Jahn–Teller effect provides an ideal framework for elucidating the correlation between photoinduced structural changes and PET reaction coordinates, thereby regulating PET dynamics in TMC-based photochemical systems.

Cu(I) diimine complexes have gained much attraction as earth abundant alternatives to noble metals in applications such as light energy conversion[29–32] and photocatalysis.[33–36] These complexes undergo a metal-to-ligand charge transfer (MLCT) transition induced by visible light excitation, causing the Cu(I) ($3d^{10}$) transiently oxidized to Cu(II) ($3d^{9}$), triggering the pseudo JTD. This symmetry-lowering distortion (*e.g.*, $D_{2d} \rightarrow D_2$ in homoleptic complexes) breaks down the degeneracy of 3d-orbitals and stabilizes the energy of MLCT state. The excited state molecular dynamics of these complexes have been detected using various ultrafast optical spectroscopies,[37–41] X-ray transient absorption spectroscopy[42] and solution scattering.[43] The JTD facilitates the access of coordinating solvent to the Cu(II) center in the MLCT state *via* reducing the angles between the two ligand planes, which lowers the MLCT state energy and enables a nonradiative decay pathway that significantly shortens the lifetime of the MLCT state.[21,22,44] In contrast, bulkier substituents attached to the 2,9-position of diimine ligands hinder the JTD in the MLCT state and thus solvent accessibility to the transient Cu(II) center, prolonging the MLCT lifetime.[44,45] Moreover, theoretical calculation have shown that the JTD has a strong effect on the magnitude of spin–orbit coupling.[46] The flattened structure (D_2 symmetry) reduces the

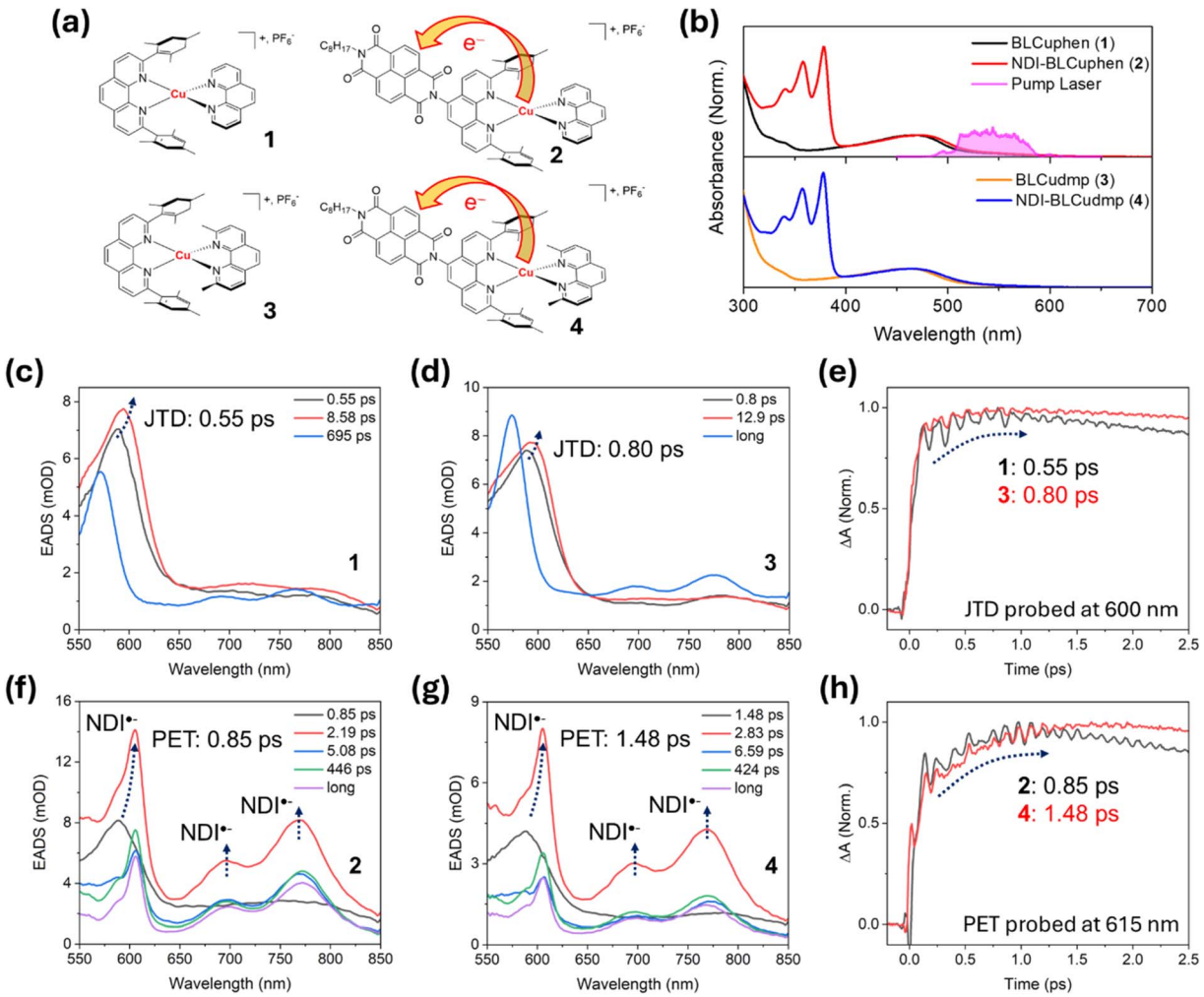

Fig. 1 (a) Schematic molecular structures for **1**–**4**. (b) Steady-state absorption and pump laser spectra. All measurements were performed in acetonitrile. (c–g) Evolution associated difference spectra (EADS) for all complexes. All spectra were obtained by global kinetic analysis on the BBTA data scanned up to 500 ps (Fig. S3 and S4). Black arrows highlight the intensity growth of excited-state absorption (ESA) related to the JTD in the ^{1}MLCT state for **1** and **3**, and the growth in the intensity of NDI anion radical band associated with the PET process for **2** and **4**. The BBTA data up to 80 fs were truncated for the global fitting in order to eliminate the contribution of coherent spike and cross-phase modulation signal around time zero. (e–h) Decay profiles probed at 600 nm near the ESA maxima (590 nm) for **1** and **3**, and at 615 nm near NDI anion radical peak (604 nm) for **2** and **4**.

spin–orbit coupling compared to the tetrahedral geometry (D_{2d} symmetry), resulting in a slower ISC rate.[23,47]

Despite its central role in the MLCT excited state dynamics, it remains largely unexplored how the photoinduced JTD in the Cu(I) diimine donor (D) influences the PET to an acceptor (A) to achieve a charge separation (CS, D^+A^-). Previous studies on Cu(I) diimine-based donor–acceptor (DA) systems, including those incorporating strong acceptor units, have primarily focused on CT energetics, kinetics and their impact on the CS lifetime, without consideration of how JTD affects the PET reaction coordinate.[30,48–51] This study aims to fill this current knowledge gap by identifying the impact of the JTD on the PET reaction coordinates, advancing our understanding and ultimately controlling the CS process in Cu(I)-based TMCs as well as other similar systems undergoing the JTD. Here, we investigate how the photoinduced JTD in the Cu(I) diimine donor (D) influences the PET to an acceptor (A) in DA dyads where D = heteroleptic Cu(I) bisphenanthroline (CuHETPHEN) complex and A = naphthalene diimide (NDI) (Fig. 1a). Recent advances in HETPHEN-based synthetic strategies have made it possible to selectively prepare heteroleptic copper bisphenanthroline complexes with well-defined asymmetry, providing a versatile platform for controlling directionality of charge displacement following the photoexcitation of MLCT state.[51–54] As reported in our previous study, the PET driven by the MLCT excitation of Ds predominantly proceeds through a mesityl-substituted phenanthroline ligand.[49] To modulate the extent of the JTD, the steric substituents at the 2,9 positions of the opposite phenanthroline ligand are varied from hydrogen (**1** and **2**) to methyl groups (**3** and **4**), enabling a direct assessment of how the structural changes affects the PET reaction coordinate. Particularly, we utilize CVWP motions to identify the PET reaction coordinate during the JTD and CS processes. Iwamura *et. al.* showed that the CVWP motions in homoleptic Cu(I) diimine complexes are a sensitive probe of the JTD trajectory.[45] The bulkier substituents slow the JTD and yield longer-lived CVWP motions due to the perturbation on the MLCT state potential energy surface (PES) near the Franck–Condon (FC) region. Katayama and co-workers used femtosecond (fs) X-ray transient absorption and scattering experiments to further demonstrated that the decoherence time for the Cu–N breathing CVWP closely correlates with the JTD rate[42,43] Building on these previous reports, we test a hypothesis that the JTD modulates the PET reaction coordinate in the DA dyads, leading to distinct CVWP signatures when comparing an increase in ligand substitution from hydrogen- to methyl-substituted DA systems. To this end, ultrafast broadband transient absorption (BBTA) spectroscopy using a 20-fs pump pulse is carried out to measure the CVWP motions and track their temporal evolution along the JTD and PET trajectories in Ds (**1** and **3**) and DAs (**2** and **4**). Ground- and excited-state normal modes and PESs for **2** and **4** are complimentary calculated to examine how the bulkier substituents influence the CVWP motions and the PES structures along the JTD coordinate. Integrating our experimental and theoretical results provides a fundamental understanding of the role of JTD in shaping the PET reaction trajectory, enabling the efficient CS in Cu(I)-based TMCs.

Results and discussion

Broadband transient absorption spectroscopy

The steady-state absorption spectra for Ds (**1** and **3**) and DAs (**2** and **4**) are presented in Fig. 1b. All complexes exhibit two ^{1}MLCT bands around 470 nm corresponding to the $S_0 \rightarrow S_2$ transition, as well as a tail extending below 500 nm for the $S_0 \rightarrow S_1$ transition.[49,55] The absorption band with distinct vibronic peaks in the 330–400 nm range for **2** and **4** originates from the NDI electron acceptor.[49] The weak π-interaction between the phenanthroline ligand and the NDI units induces a small redshift in the ^{1}MLCT bands of **2** and **4** compared to those of **1** and **3**. The BBTA measurements were performed using the 20-fs pump pulses with the spectrum covering the lowest ^{1}MLCT band (Fig. 1b). The BBTA kinetics were analyzed by the global kinetic fitting with a sequential model using Glotaran package (Fig. 1c–h).[56] Evolution associated difference spectra (EADS) for **1** and **3** exhibit early rise kinetics (black → red EADSs) corresponding to the intensity-growth and redshift of excited state absorption (ESA) associated with the ^{1}MLCT excited state dynamics (Fig. 1c–e). The rise dynamics are attributed to the JTD triggered by the ^{1}MLCT excitation.[45] The JTD time constants are 0.55 ps in **1** and 0.80 ps in **3**. The bulkier methyl substituents in **3** introduce the steric hindrance with the mesityl groups in the opposite phenanthroline ligand. This enhanced steric congestion restricts the ligand-flattening motion, resulting in the slower JTD process. Following the JTD, the ISC (~10 ps) from the singlet to triplet MLCT states is manifested by a blue-shift and narrowing of ESA spectra (red → blue EADSs).[55] For **2** and **4**, the EADSs in early time clearly show the temporal evolution of the ESA spectra from the ^{1}MLCT-like shape (black EADS) to the NDI radical anion spectrum (red EADS) featuring the characteristic peaks at 607, 695 and 775 nm (Fig. 1f and g).[57] This spectral change confirms that PET occurs from CuHEPTHEN to NDI. The early-time BBTA spectra of **2** and **4** closely resemble the ESA of the initially populated ^{1}MLCT state observed in **1** and **3** (Fig. 1c–g). The spectral similarity indicates that the initial excited-state character and the PET process are not significantly perturbed by the weak electronic coupling between the phenanthroline ligand and the NDI unit. Notably, the PET rate is comparable to the JTD rate, indicating that the two processes occur concomitantly. Interestingly, the bulkier methyl substituents on the 2,9-phenanthroline positions not only prolong the JTD rate, but also the PET time constants from 0.85 ps in **2** to 1.48 ps in **4** (Fig. 1h), which suggests that the PET process is closely correlated with the JTD dynamics. At longer time delays, PET is followed by multiple relaxation processes including ISC and charge recombination as reported in our previous work.[49] In the present study, we focus on the early kinetics up to 2.5 ps to investigate the interplay between the JTD and PET dynamics.

Fast Fourier transformation

The CVWP motions were extracted as oscillatory residuals after removing the population evolution from the BBTA time profiles (Fig. 2a–c and S5). Fast Fourier transformation (FFT) of these

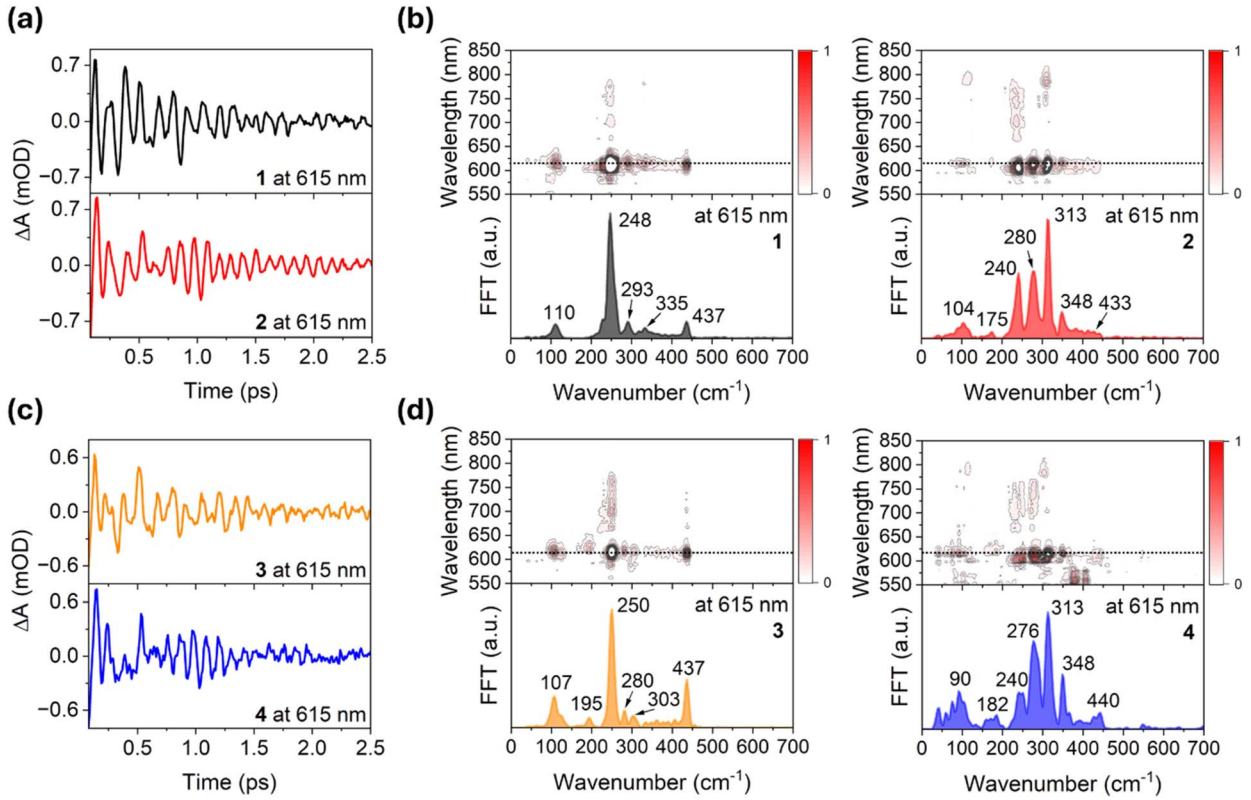

Fig. 2 (a–c) Beating signals detected at 615 nm. (b–d) 2D-contour FFT maps (top) and FFT amplitude spectra at 615 nm (bottom).

beating signals reveals the CVWP frequencies below 700 cm^{-1} (Fig. 2b–d). For **1** and **3**, the dominant peak in the FFT amplitude spectra is around 250 cm^{-1} with smaller features around 110, 290, 330 and 435 cm^{-1}, which correspond to the FC-active CVWP modes populated in the ^{1}MLCT state of Ds. Although the ^{1}MLCT states of the Ds are selectively excited, **2** and **4** display strikingly distinct FFT amplitude spectra compared to **1** and **3**. While the ~110 and ~250 cm^{-1} CVWPs in **1** and **3** downshift slightly to ~100 and ~240 cm^{-1}, a strong FFT band at 313 cm^{-1} emerges in **2** and **4**. Additionally, the sharp 437 cm^{-1} peaks observed in **1** and **3** become significantly broadened in **2** and **4**. These pronounced spectral changes in the DAs demonstrate that PET, rather than the FC-active ^{1}MLCT nuclear motion, dominates the CVWP dynamics in **2** and **4.**

Short-time Fourier transformation

To track the temporal evolution of vibrational frequencies and amplitudes during the JTD and PET processes, we performed short-time Fourier transform (STFT) analysis on the CVWP oscillations of Ds and DAs monitored at 615 nm (Fig. 3). In this analysis, a 1-ps FFT window was used and slid with a 100-fs step over the pump–probe delay from 0.08 to 1.48 ps. For example, the STFT spectrum at 0.08 ps corresponds to the FFT of CVWP oscillations between 0.08 and 1.08 ps and the STFT spectrum at 1.48 ps corresponds to the response between 1.48 and 2.48 ps. As shown in Fig. 3a–c, the STFT spectra for **1** and **3** largely maintain their overall spectral profiles as the CVWP motions decay in amplitudes. As compared to the FFT results, the CVWP peaks near 110, 250, and 437 cm^{-1} show no discernible frequency shifts and no substantial redistribution of relative amplitudes over time, indicating that the JTD does not significantly perturb either the frequencies or relative amplitudes of these CVWP motions. In contrast, **2** and **4** exhibit significant spectral evolution during the PET process (Fig. 3b–d). At 0.08 ps, the STFT spectra contain the CVWP peaks near 100, 240, and 435 cm^{-1}, accompanied by enhanced amplitudes at the 280 and 313 cm^{-1} modes that are clearly different from those of **1** and **3**. The altered amplitude distribution at early times indicates that the CVWPs around 100, 240, 280 and 435 cm^{-1} undergo rapid decoherence within the 1-ps window. Specifically, the amplitudes of these modes decrease sharply in the STFT spectra at 0.28 and 0.38 ps, which are substantially faster than the JTD-induced damping of the CVWP motions observed in **1** and **3**. This result demonstrates that the rapid dephasing originates from the PET rather than the JTD. Notably, the vibrational feature near 313 cm^{-1} emerges as the dominant vibrational feature in the STFT spectra while other modes completely dephase. The newly formed 313 cm^{-1} CVWP decays during CS, with faster dephasing observed for **4** relative to **2**, resulting in an observable 313 cm^{-1} signal for **2** at 1.48 ps in the STFT spectrum. The strong time-dependent spectral evolution in the STFT spectra of **2** and **4** reveals that the PET governs the ultrafast decoherence of FC-active CVWP modes in the ^{1}MLCT and promotes the emergence of a dominant CVWP motion near 313 cm^{-1}.

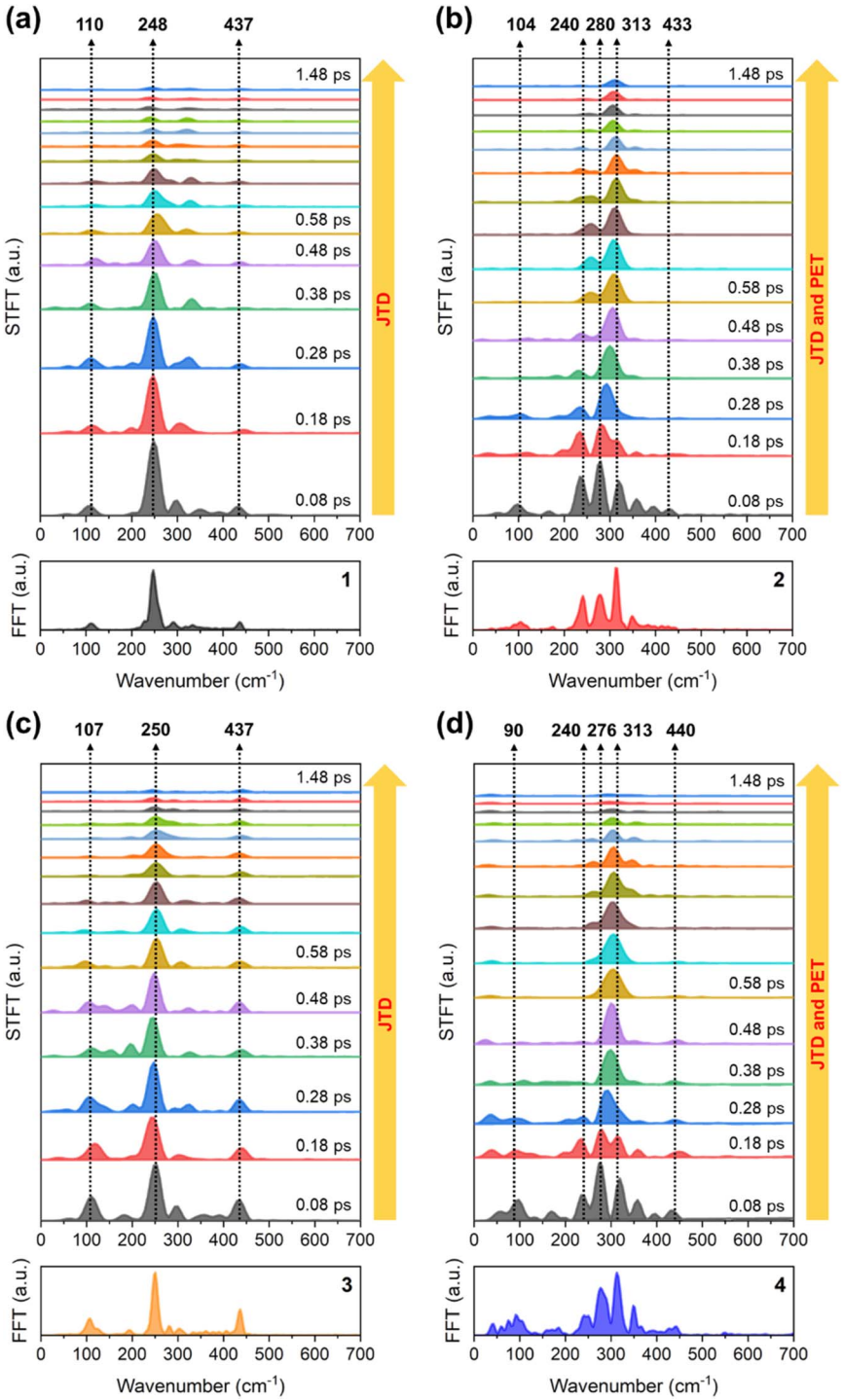

Fig. 3 The STFT results for **1–4** (a–d) (Top): STFT amplitude spectra of the beating signals detected at 615 nm, plotted as a function of pump–probe delay time from 0.08 to 1.48 ps. The 1-ps STFT window is slid with 100-fs increments; and bottom: FFT amplitude spectra obtained from the same beating signals over the entire pump–probe delay range (0.08–2.5 ps).

Fourier filtering

To correlate the CVWP motions with the spectral evolution of BBTA data, we conducted Fourier filtering analysis on the observed CVWP oscillations in the range of 0–700 cm^{-1} (Fig. 4a, b, 5a, b, S6 and S7). Specific FFT bands were selectively filtered out using a super-Gaussian function, and inverse Fourier transformation retrieved the filtered frequency domain data back to the time domain.[58] This approach extracted the phase-flip (PF) position for each oscillation from overlapping raw beating signals. The PF of CVWP motion occurs near the PES energy minimum. In ultrafast optical TA spectroscopy, the excited state CVWP shows the PFs around ESA or stimulated

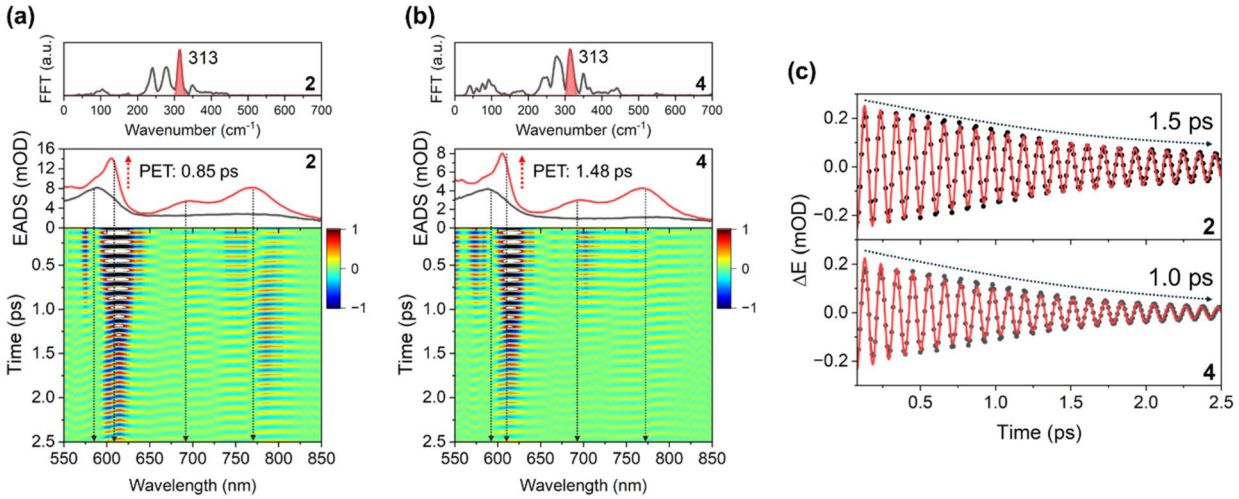

Fig. 4 (a and b) Top: FFT spectra at 615 nm. The red-shaded bands indicate Fourier-filtered frequencies obtained by a super-Gaussian window. Middle: EADSs associated with PET. (Bottom): Fourier-filtered oscillation maps for ~313 cm^{-1} CVWP motions. The dotted arrows highlight the correlation between the peak wavelengths of ^{1}MLCT ESA and NDI radical anion, and the PF wavelengths. (c) Fourier-filtered CVWP oscillations (black dotted lines) at 615 nm for the ~313 cm^{-1} CVWPs for **2** and **4**. The red solid lines show the fitting results obtained by a single exponentially damped sine function.

emission maxima, while the PF for the ground state CVWP oscillation appears around GS bleaching maximum.[59] Thus, correlating the PF positions with the TA spectral maxima enables the assignment of the electronic state from which the CVWP originates.

As shown in Fig. 4a, the PFs of the 313 cm^{-1} CVWP in **2** are observed near 580, 607, 695, and 775 nm. In the spectral region from 550 to 625 nm where the MLCT-like ESA (black EADS) overlaps with the NDI anion absorption (red EADS), the early-time PF appears predominantly near 580 nm, corresponding to the maximum of the MLCT-like ESA. In contrast, no PF is detected near 607 nm, the maximum of the NDI anion absorption. However, the PF near 607 nm emerges at ~0.6–0.7 ps and becomes increasingly pronounced at later times. This temporal evolution of the oscillation pattern indicates that the 313 cm^{-1} CVWP initially modulates the MLCT-like ESA and subsequently couples to the NDI anion absorption as the PET proceeds. Combined with the STFT spectral changes for **2** and **4**, the delayed appearance of PFs at the NDI anion peaks indicates that the 313 cm^{-1} CVWP propagates from the ^{1}MLCT state to the CS manifold. A similar PF pattern is observed for **4** (Fig. 4b). However, the PF features at the NDI anion peaks (607, 695, and 775 nm) are significantly weaker, while the PF near the MLCT ESA maximum remains clearly visible at early times. This behavior arises from faster vibrational decoherence in **4**, as illustrated in Fig. 4c. The damping times of the Fourier-filtered 313 cm^{-1} oscillations monitored at 615 nm were obtained by fitting a single exponentially damped sine function, yielding the decay constants of 1.5 ps for **2** and 1.0 ps for **4**. The shorter damping time in **4** indicates more rapid dephasing of the 313 cm^{-1} CVWP as it evolves along the PET trajectory. This is consistent with the STFT results that the discernible 313 cm^{-1} amplitude persists in the STFT spectrum of **2** at 1.48 ps, whereas no such feature is observed for **4** (Fig. 3). Interestingly, when compared with the PET timescale, the dephasing times of the 313 cm^{-1} mode do not follow the expected trend in which bulkier methyl substituents in **4** slow the PET while concomitantly prolonging the CVWP decoherence time. Instead, increasing steric bulk lengthens the PET time but shortens the 313 cm^{-1} CVWP dephasing time. Moreover, the damping time of the 313 cm^{-1} CVWP in **2** is approximately 2 times longer than its PET time. These results suggest that the decoherence of the 313 cm^{-1} mode is not governed by the PET process itself but arises from a distinct vibrational decoherence mechanism.

To gain further insight into this mechanism, we extended the Fourier filtering analysis on other vibrations near 100, 240, and 280 cm^{-1} (440 cm^{-1} CVWPs were too weak to reliably resolve PFs). The 240 and 280 cm^{-1} CVWPs in **2** and **4** exhibit oscillation patterns and PF positions similar to the ~250 cm^{-1} CVWPs observed in **1** and **3**, indicating that these CVWP modes decohere within the ^{1}MLCT PES during the CS process (Fig. S6). However, the low-frequency CVWPs near 100 cm^{-1} display totally different behavior. For **1** and **3**, the ~110 cm^{-1} CVWP exhibits clear PFs near the maximum of the MLCT ESA (Fig. 5a and S7a), identifying this mode as the FC-active MLCT nuclear motion. In contrast, for **2** and **4**, the ~100 cm^{-1} CVWP exhibits pronounced PFs at the NDI anion absorption peaks near 607, 695, and 775 nm (Fig. 5b and S7b). Particularly, the PF near 607 nm appears immediately following MLCT excitation and decays rapidly, in sharp contrast to the delayed PF evolution observed for the 313 cm^{-1} CVWP. Although the early-time BBTA spectra are dominated by the MLCT-like ESA (black EADS), the ~100 cm^{-1} CVWPs in **2** and **4** selectively modulate the NDI anion absorption features. The immediate modulation of the NDI anion absorption by the ~100 cm^{-1} CVWP strongly suggests that this low-frequency vibration actively drives nonadiabatic mixing between the ^{1}MLCT and CS states by periodically modulating their electronic coupling. This vibronic

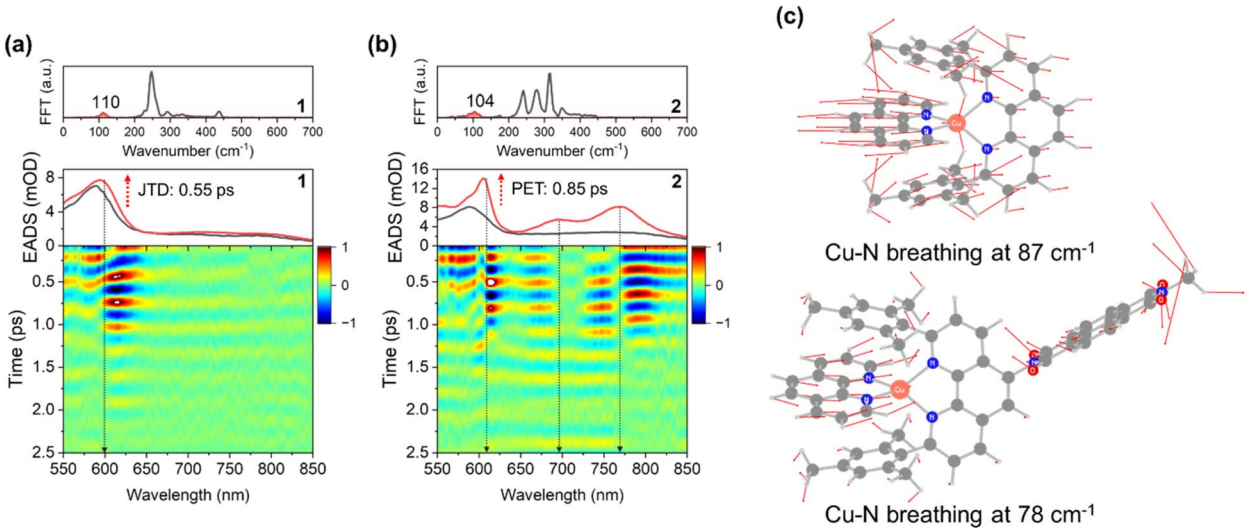

Fig. 5 (a and b) Top: FFT spectra at 615 nm. The red-shaded bands indicate Fourier-filtered frequencies obtained by a super-Gaussian window. Middle: EADSs associated with JTD for **1** and PET for **2**. (Bottom): Fourier-filtered oscillation maps for ~110 cm^{-1} CVWP for **1** and ~104 cm^{-1} CVWP for **2**. The dotted arrows highlight the correlation between the peak wavelengths of ^{1}MLCT ESA and NDI radical anion, and the PF wavelengths. (c) Calculated Cu–N breathing vibrations in the ground state for **1** (top) and **2** (bottom).

motion indicates that the ~100 cm^{-1} vibration is an effective reaction coordinate for the PET that is distinct from the FC-active MLCT vibrational modes at 240 and 280 cm^{-1}. Furthermore, it is reasonably expected that this low-frequency vibronic motion significantly influences the evolution and decoherence of the 313 cm^{-1} CVWP along the PET reaction trajectory.

Normal mode analysis

To elucidate the origin and role of the ~100 cm^{-1} vibronic motion, we calculated the normal modes for the optimized ground state (GS) and lowest ^{1}MLCT states of Ds and DAs. In all complexes, breathing vibrational motions *via* the bond distance change between Cu and ligated Ns (Cu–N) are observed near 100 cm^{-1} as illustrated in Fig. 5c, S7c and S8. The Cu–N breathing CVWP motion was observed in homoleptic Cu(I) diimine complexes and can be readily launched by ultrafast FC excitation.[42,43,45] Upon ^{1}MLCT photoexcitation, Cu(I) is transiently oxidized to Cu*(II), which drives a contraction of the Cu–N bonds due to both the antibonding character of the d orbitals involved in the ^{1}MLCT transition and the increased electrostatic attraction between the oxidized Cu center and the phenanthroline ligands.[40,46] Consistent with previous reports on homoleptic Cu(I) diimine complexes, our calculations show a significant shortening of the average Cu–N bond length upon ^{1}MLCT excitation (Table 1). For all DAs, the Cu–N contraction from the GS to the ^{1}MLCT state is 0.012 Å. In addition, the equilibrium Cu–N bond length in both the GS and ^{1}MLCT is ~0.01 Å shorter in **2** than in **4**, indicating that the increased steric repulsion imposed by the bulkier methyl substituents hinder the Cu–N contraction around the Cu center.

Importantly, in the DA dyads, the calculated ~100 cm^{-1} modes involve not only the Cu–N breathing motions but also concerted displacement of the NDI moiety. This collective vibration modulates the instantaneous distance between the positively charged Cu center and the negatively charged phenanthroline ligand and NDI. As summarized in Table 1, Fig. S9 and S10, the Cu–N breathing motion periodically alters the distance between Cu center and NDI by 0.101 Å for **2** and 0.147 Å for **4** in GS and by 0.085 Å for **2** and 0.033 Å for **4** in the ^{1}MLCT state. Periodic contraction and expansion of the Cu–N bonds dynamically modulate the Cu–NDI distance, leading to a time-dependent alternation in both the electrostatic and electronic interactions between Cu center and NDI acceptor. In this context, the experimental observation that this CVWP motion immediately modulates the NDI anion absorption (Fig. 5b and S7b), despite the BBTA spectra being initially dominated by MLCT-like ESA, can be rationalized by this vibronic motion

Table 1 Calculated average Cu–N bond lengths and Cu–NDI distance modulations induced by the Cu–N breathing vibration

	[a]Cu–N Avg in GS (Å)	[a]Cu–N Avg in ^{1}MLCT (Å)	[b]Cu–NDI distance modulation in GS (Å)	[b]Cu–NDI distance modulation in ^{1}MLCT (Å)
2	2.051	2.039	0.101	0.085
4	2.061	2.049	0.147	0.033

[a] Cu–N bond lengths are averaged over the four Cu–N bonds in CuHETPHENs (Ds). [b] Cu-NDI distances are measured from Cu atom to the nearest N atom of NDI. The distance modulation is calculated as the change in the Cu-NDI distance between the compressed and expanded geometries along the Cu–N breathing vibration.

periodically modulating the electronic coupling between D and A. Such modulation transiently alters the electronic population and charge density on the NDI acceptor. Therefore, rather than serving merely as a spectator FC-active MLCT mode, the ~100 cm^{-1} vibration acts as a vibronically active coordinate that modulates the D–A electronic coupling and facilitates ultrafast PET.

Potential energy surface calculations

To further understand how the JTD influences the vibronic motion and the subsequent CS dynamics, we calculated the PESs of the GS, ^{1}MLCT, and CS states as a function of the dihedral angle between two N–Cu–N planes (Fig. 6). In the GS, the PESs exhibit global minima at 80° and 100° for **2**, and at 75° and 105° for **4**. The energy at 90° is only slightly higher than these minima and remains below thermal energy at room temperature, indicating a broad distribution of thermally accessible conformations that can be excited by the pump pulse spanning the MLCT absorption band (Fig. 1b). In contrast, the PESs of the ^{1}MLCT state (green solid lines in Fig. 6) display pronounced global minima near ~65° and ~115° for both **2** and **4**, reflecting the JTD toward the flattened geometry. Similar minima are found for the lowest CS states (red dotted lines in Fig. 6). Notably, a higher-lying CS state (blue dotted lines in Fig. 6) exhibits distinct PES shape along the JTD coordinate, with minima near 90° and increasing energy upon flattening. These higher-lying CS states for **2** and **4** correspond to a transition from HOMO−1 (Cu 3d) to LUMO (NDI), whereas the lowest CS state originates from the HOMO (Cu 3d) → LUMO transition (Fig. S11 and S12). As the dihedral angle changes, the HOMO energy increases while the HOMO−1 energy decreases, leading to opposite energetic shifts of the lowest and higher-lying CS states. As a result, the higher-lying CS state crosses the ^{1}MLCT state near ~75° (~105°) during the JTD process. This PES topology indicates that the PET process from the ^{1}MLCT state initially accesses the higher-lying CS state during the JTD, followed by relaxation to the lowest CS state. Access to this higher-lying CS state accelerates the CS process relative to the direct transition from the ^{1}MLCT state to the lowest CS state. As a result, the FC-active MLCT vibrational modes (110, 240, 280, and 440 cm^{-1}) decohere more rapidly than the JTD-driven structural evolution, observed in the STFT analysis for both **2** and **4**.

The excited state PES calculations also reveal that the shape of the ^{1}MLCT PES near 90° differs markedly between **2** and **4**.

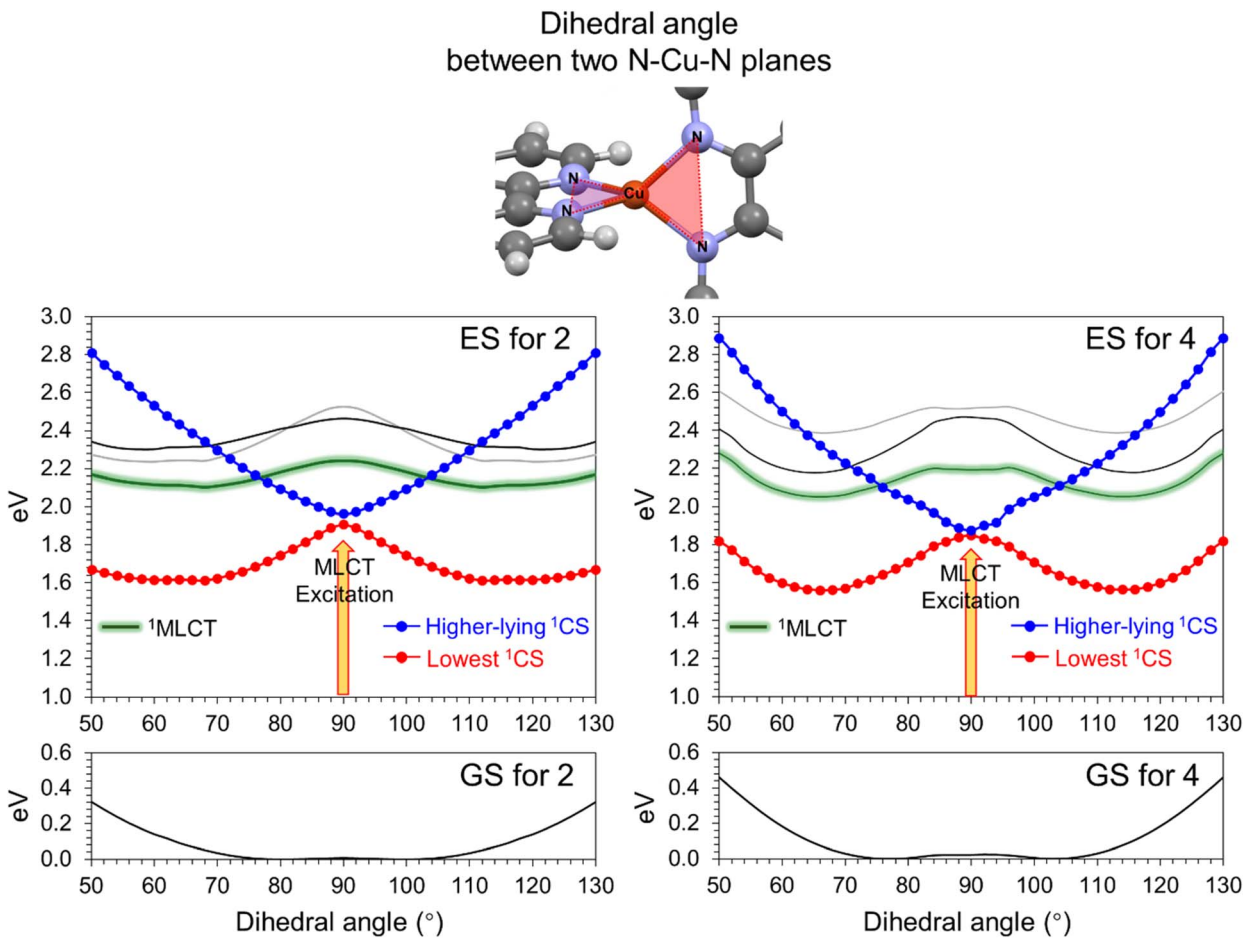

Fig. 6 Calculated PESs of the ground, ^{1}MLCT, and ^{1}CS states for **2** (left) and **4** (right) as a function of the dihedral angle between two N–Cu–N planes. The solid green line highlights the lowest ^{1}MLCT state, while the blue and red dotted lines represent the higher-lying and lowest ^{1}CS states, respectively.

For **2**, the PES exhibits the maximum at 90°, driving the JTD immediately following the MLCT excitation. In contrast, the PES for **4** is significantly flatter between 80° and 100°, with a shallow local minimum near 90°, attributable to steric hindrance between the mesityl and methyl substituents. This behavior is consistent with previously reported PESs for homoleptic Cu(I) bisphenanthroline complexes bearing bulky substituents.[40,45] The steric effect in the ^{1}MLCT PESs plays a critical role in regulating the ~100 cm^{-1} vibronic motion. As the JTD flattens the Cu coordination geometry upon MLCT excitation, the 2,9-phenanthroline substituents approach more closely than in the GS, substantially increasing steric repulsion in the excited state, particularly in **4**. This enhanced steric hindrance restricts the extent of Cu–N bond length modulation during the Cu–N breathing vibration. Quantitatively, **2** exhibits only a modest reduction in Cu–NDI distance modulation from 0.102 Å in the GS to 0.085 Å in the ^{1}MLCT state, whereas **4** shows a dramatic suppression from 0.147 Å (GS) to 0.033 Å (^{1}MLCT) (Table 1). These results indicate that modulation of the Cu–NDI distance by the Cu–N breathing motion is substantially weakened in **4** relative to **2** as the JTD progresses. Thus, the ~100 cm^{-1} vibronic motion in **4** becomes significantly less effective at modulating the D–A electronic coupling near the PES crossing region between the ^{1}MLCT and higher-lying CS states. This reduced vibronic coupling leads to slower CS process in **4** compared to **2**. In contrast, stronger vibronic coupling in **2** near the PES crossing region enables partial delocalization of the electronic wavefunction between the phenanthroline ligand and the NDI acceptor, promoting faster electron transfer from the ^{1}MLCT to the high-lying CS state than in the sterically bulky **4**. Importantly, this difference in vibronic coupling strength also rationalizes the observed coherence behavior of the higher-frequency 313 cm^{-1} CVWP. In **2**, enhanced vibronic coupling at the crossing region facilitates more coherent passage through the PES intersection, allowing the 313 cm^{-1} wavepacket to retain coherence during the ^{1}MLCT-to-CS transition. In **4**, however, weaker vibronic coupling leads to inefficient state mixing, resulting in the rapid loss of 313 cm^{-1} coherence, and the overall slower CS process.

Collectively, our findings strongly suggest that JTD-driven structural evolution induces conical intersection dynamics during the PET process. Along the JTD coordinate, the electronic degeneracy between the ^{1}MLCT and CS electronic states is achieved, while the Cu–N breathing motion acts as a key vibronic coupling coordinate that dynamically modulates the D–A electronic coupling and enables efficient nonadiabatic PET. The interplay between the JTD-controlled PES trajectory and the Cu–N breathing nuclear motion ultimately governs the CS dynamics in these Cu(I)-based DA systems.

Conclusion

In summary, this work uncovers a vibronic mechanism underlying in the PET process in Cu(I)-based DA systems by directly linking the JTD dynamics with the electronic coupling between D and A. Using the CVWP measurements in combination with normal modes and PES calculations, we identify the Cu–N breathing mode (~100 cm^{-1}) as a key vibronic coupling coordinate that dynamically modulates D–A electronic coupling and enables ultrafast nonadiabatic mixing between the ^{1}MLCT and CS states. The JTD defines the reaction coordinate that brings these electronic states into degeneracy, while the vibronic motion at this crossing determines whether the CS proceeds coherently and efficiently. Importantly, steric modulation of the ligand framework selectively suppresses this vibronic coupling in the excited state, leading to faster vibrational decoherence, reduced electronic mixing, and slower CS. These results establish that the CS efficiency in Cu(I) DA complexes is not dictated solely by energetic alignment, but by specific vibronic coordinates at the conical intersection along the PET reaction pathway. Thus, our findings open new possibilities for controlling PET through targeted vibrational and structural design, providing design principles for optimizing Cu-based photosensitizers and molecular systems for solar energy conversion and photochemical applications.

Author contributions

PK and BTP: performed the ultrafast BBTA experiments. PK: analyzed the BBTA kinetics and CVWP dynamics and wrote the manuscript. PK, KLM, and LXC: conceptualized and supervised the project and reviewed and edited the manuscript. LK and KLM: performed the synthesis and characterization. XY and XL: performed the computations and wrote the computational methodology.

Conflicts of interest

There are no conflicts to declare.

Data availability

The datasets generated during and/or analysed during the current study are not publicly available but are available from the authors on reasonable request.

Supplementary information (SI) is available. See DOI: https://doi.org/10.1039/d5sc10209j.

Acknowledgements

P. K., X. Y., B. T. P., L. K., X. L., K. L. M. and L. X. C. as well as computational work are supported by the Ultrafast Initiative of the U. S. Department of Energy, Office of Science, Office of Basic Energy Sciences, through Argonne National Laboratory under Contract No. DE-AC02-06CH11357. The development of computational method for simulating excited state dynamics is supported by the National Science Foundation (CHE-1856210 to X.L).

References

1 D. M. Schultz and T. P. Yoon, *Science*, 2014, **343**, 1239176.
2 C. E. Housecroft and E. C. Constable, *Chem. Sci.*, 2022, **13**, 1225–1262.

3 L. Lindh, P. Chábera, N. W. Rosemann, J. Uhlig, K. Wärnmark, A. Yartsev, V. Sundström and P. Persson, *Catalysts*, 2020, **10**, 315.
4 J. Twilton, C. Le, P. Zhang, M. H. Shaw, R. W. Evans and D. W. C. MacMillan, *Nat. Rev. Chem.*, 2017, **1**, 0052.
5 K. P. S. Cheung, S. Sarkar and V. Gevorgyan, *Chem. Rev.*, 2022, **122**, 1543–1625.
6 H. Kumagai, Y. Tamaki and O. Ishitani, *Acc. Chem. Res.*, 2022, **55**, 978–990.
7 D. Kim, V. Q. Dang and T. S. Teets, *Chem. Sci.*, 2024, **15**, 77–94.
8 D. M. Arias-Rotondo and J. K. McCusker, *Chem. Soc. Rev.*, 2016, **45**, 5803–5820.
9 G. Auböck and M. Chergui, *Nat. Chem.*, 2015, **7**, 629–633.
10 H. T. Lemke, K. S. Kjær, R. Hartsock, T. B. van Driel, M. Chollet, J. M. Glownia, S. Song, D. Zhu, E. Pace, S. F. Matar, M. M. Nielsen, M. Benfatto, K. J. Gaffney, E. Collet and M. Cammarata, *Nat. Commun.*, 2017, **8**, 15342.
11 J. D. Gaynor, J. Sandwisch and M. Khalil, *Nat. Commun.*, 2019, **10**, 5621.
12 P. Kim, A. J. S. Valentine, S. Roy, A. W. Mills, F. N. Castellano, X. Li and L. X. Chen, *Faraday Discuss.*, 2022, **237**, 259–273.
13 S. R. Rather, N. P. Weingartz, S. Kromer, F. N. Castellano and L. X. Chen, *Nature*, 2023, **620**, 776–781.
14 P. Kim, A. J. S. Valentine, S. Roy, A. W. Mills, A. Chakraborty, F. N. Castellano, X. Li and L. X. Chen, *J. Phys. Chem. Lett.*, 2021, **12**, 6794–6803.
15 D. Leshchev, A. J. S. Valentine, P. Kim, A. W. Mills, S. Roy, A. Chakraborty, E. Biasin, K. Haldrup, D. J. Hsu, M. S. Kirschner, D. Rimmerman, M. Chollet, J. M. Glownia, T. B. van Driel, F. N. Castellano, X. Li and L. X. Chen, *Angew. Chem., Int. Ed.*, 2023, **62**, e202304615.
16 K. Kunnus, M. Vacher, T. C. B. Harlang, K. S. Kjær, K. Haldrup, E. Biasin, T. B. van Driel, M. Pápai, P. Chabera, Y. Liu, H. Tatsuno, C. Timm, E. Källman, M. Delcey, R. W. Hartsock, M. E. Reinhard, S. Koroidov, M. G. Laursen, F. B. Hansen, P. Vester, M. Christensen, L. Sandberg, Z. Németh, D. S. Szemes, É. Bajnóczi, R. Alonso-Mori, J. M. Glownia, S. Nelson, M. Sikorski, D. Sokaras, H. T. Lemke, S. E. Canton, K. B. Møller, M. M. Nielsen, G. Vankó, K. Wärnmark, V. Sundström, P. Persson, M. Lundberg, J. Uhlig and K. J. Gaffney, *Nat. Commun.*, 2020, **11**, 634.
17 B. C. Paulus, S. L. Adelman, L. L. Jamula and J. K. McCusker, *Nature*, 2020, **582**, 214–218.
18 H. A. Jahn, E. Teller and F. G. Donnan, *Proc. R. Soc. Lond., Ser. A Math. Phys. Sci.*, 1997, **161**, 220–235.
19 I. B. Bersuker, *Chem. Rev.*, 2001, **101**, 1067–1114.
20 H. Köppel, D. R. Yarkony and H. Barentzen, *The Jahn-Teller Effect: Fundamentals and Implications for Physics and Chemistry*, Springer Science & Business Media, 2009.
21 L. Kohler, R. G. Hadt, D. Hayes, L. X. Chen and K. L. Mulfort, *Dalton Trans.*, 2017, **46**, 13088–13100.
22 F. N. Castellano and M. C. Rosko, *Acc. Chem. Res.*, 2024, **57**, 2872–2886.
23 V. Tiwari, M. Gallagher-Jones, H. Hwang, H.-G. Duan, A. I. Kirkland, R. J. D. Miller and A. Jha, *ACS Phys. Chem. Au*, 2024, **4**, 660–668.
24 F. Liedy, J. Eng, R. McNab, R. Inglis, T. J. Penfold, E. K. Brechin and J. O. Johansson, *Nat. Chem.*, 2020, **12**, 452–458.
25 R. Phelps, E. Agapaki, E. K. Brechin and J. O. Johansson, *Chem. Sci.*, 2024, **15**, 11956–11964.
26 M. Hervé, B. Marekha, S. Mazerat, T. Mallah, M. Cammarata, S. F. Matar, S. Haacke, J. Léonard and E. Collet, *Mater. Adv.*, 2024, **5**, 3357–3366.
27 S. E. Canton, M. Biednov, M. Pápai, F. A. Lima, T.-K. Choi, F. Otte, Y. Jiang, P. Frankenberger, M. Knoll, P. Zalden, W. Gawelda, A. Rahaman, K. B. Møller, C. Milne, D. J. Gosztola, K. Zheng, M. Retegan and D. Khakhulin, *Advanced Science*, 2023, **10**, 2206880.
28 J. T. Malme, J. N. Weaver, G. S. Girolami and J. Vura-Weis, *Inorg. Chem.*, 2024, **63**, 13825–13830.
29 C. E. Housecroft and E. C. Constable, *Chem. Soc. Rev.*, 2015, **44**, 8386–8398.
30 M. W. Mara, D. N. Bowman, O. Buyukcakir, M. L. Shelby, K. Haldrup, J. Huang, M. R. Harpham, A. B. Stickrath, X. Zhang, J. F. Stoddart, A. Coskun, E. Jakubikova and L. X. Chen, *J. Am. Chem. Soc.*, 2015, **137**, 9670–9684.
31 M. Sandroni, Y. Pellegrin and F. Odobel, *C. R. Chim.*, 2016, **19**, 79–93.
32 D. Franchi, V. Leandri, A. R. P. Pizzichetti, B. Xu, Y. Hao, W. Zhang, T. Sloboda, S. Svanström, U. B. Cappel, L. Kloo, L. Sun and J. M. Gardner, *ACS Appl. Energy Mater.*, 2022, **5**, 1460–1470.
33 C. B. Larsen and O. S. Wenger, *Chem.–Eur. J.*, 2018, **24**, 2039–2058.
34 X. Zhang, M. Cibian, A. Call, K. Yamauchi and K. Sakai, *ACS Catal.*, 2019, **9**, 11263–11273.
35 J. Beaudelot, S. Oger, S. Peruško, T.-A. Phan, T. Teunens, C. Moucheron and G. Evano, *Chem. Rev.*, 2022, **122**, 16365–16609.
36 Y. Abderrazak and O. Reiser, *Curr. Opin. Green Sustainable Chem.*, 2025, **52**, 100998.
37 G. B. Shaw, C. D. Grant, H. Shirota, E. W. Castner, G. J. Meyer and L. X. Chen, *J. Am. Chem. Soc.*, 2007, **129**, 2147–2160.
38 M. Iwamura, S. Takeuchi and T. Tahara, *J. Am. Chem. Soc.*, 2007, **129**, 5248–5256.
39 M. Iwamura, S. Takeuchi and T. Tahara, *Phys. Chem. Chem. Phys.*, 2014, **16**, 4143–4154.
40 M. Iwamura, H. Watanabe, K. Ishii, S. Takeuchi and T. Tahara, *J. Am. Chem. Soc.*, 2011, **133**, 7728–7736.
41 L. Hua, M. Iwamura, S. Takeuchi and T. Tahara, *Phys. Chem. Chem. Phys.*, 2015, **17**, 2067–2077.
42 T. Katayama, T. Northey, W. Gawelda, C. J. Milne, G. Vankó, F. A. Lima, R. Bohinc, Z. Németh, S. Nozawa, T. Sato, D. Khakhulin, J. Szlachetko, T. Togashi, S. Owada, S.-i. Adachi, C. Bressler, M. Yabashi and T. J. Penfold, *Nat. Commun.*, 2019, **10**, 3606.
43 T. Katayama, T.-K. Choi, D. Khakhulin, A. O. Dohn, C. J. Milne, G. Vankó, Z. Németh, F. A. Lima, J. Szlachetko,

T. Sato, S. Nozawa, S.-i. Adachi, M. Yabashi, T. J. Penfold, W. Gawelda and G. Levi, *Chem. Sci.*, 2023, **14**, 2572–2584.
44 M. W. Mara, K. A. Fransted and L. X. Chen, *Coord. Chem. Rev.*, 2015, **282–283**, 2–18.
45 M. Iwamura, S. Takeuchi and T. Tahara, *Acc. Chem. Res.*, 2015, **48**, 782–791.
46 Z. A. Siddique, Y. Yamamoto, T. Ohno and K. Nozaki, *Inorg. Chem.*, 2003, **42**, 6366–6378.
47 S. Garakyaraghi, E. O. Danilov, C. E. McCusker and F. N. Castellano, *J. Phys. Chem. A*, 2015, **119**, 3181–3193.
48 M. Ruthkosky, C. A. Kelly, M. C. Zaros and G. J. Meyer, *J. Am. Chem. Soc.*, 1997, **119**, 12004–12005.
49 D. Hayes, L. Kohler, L. X. Chen and K. L. Mulfort, *J. Phys. Chem. Lett.*, 2018, **9**, 2070–2076.
50 B. T. Phelan, Z.-L. Xie, X. Liu, X. Li, K. L. Mulfort and L. X. Chen, *J. Chem. Phys.*, 2024, **160**, 144905.
51 S. A. Roget, W. C. Henke, M. Taub, P. Kim, J. T. Yarranton, X. Li, K. L. Mulfort and L. X. Chen, *Photochem*, 2025, **5**, 16.
52 M. Schmittel and A. Ganz, *Chem. Commun.*, 1997, 999–1000, DOI: 10.1039/A701509G.
53 L. Wang, Z.-L. Xie, B. T. Phelan, V. M. Lynch, L. X. Chen and K. L. Mulfort, *Inorg. Chem.*, 2023, **62**, 14368–14376.
54 M. C. Rosko, J. P. Wheeler, R. Alameh, A. P. Faulkner, N. Durand and F. N. Castellano, *Inorg. Chem.*, 2024, **63**, 1692–1701.
55 L. Kohler, D. Hayes, J. Hong, T. J. Carter, M. L. Shelby, K. A. Fransted, L. X. Chen and K. L. Mulfort, *Dalton Trans.*, 2016, **45**, 9871–9883.
56 J. J. Snellenburg, S. Laptenok, R. Seger, K. M. Mullen and I. H. M. van Stokkum, *J. Stat. Software*, 2012, **49**, 1–22.
57 S. V. Bhosale, C. H. Jani and S. J. Langford, *Chem. Soc. Rev.*, 2008, **37**, 331–342.
58 C. Fitzpatrick, J. H. Odhner and R. J. Levis, *J. Phys. Chem. A*, 2020, **124**, 6856–6866.
59 S. R. Rather and G. D. Scholes, *J. Phys. Chem. A*, 2016, **120**, 6792–6799.